Tri-directional Gradient Operators for Hexagonal Image Processing

Sonya Coleman[1], Bryan Scotney[2] and Bryan Gardiner[1]

[1] *University of Ulster, Magee, Londonderry, BT48 7JL, Northern Ireland, UK*

[2] *University of Ulster, Coleraine, BT52 1SA, Northern Ireland, UK*

{sa.coleman, bw.scotney, b.gardiner}@ulster.ac.uk

Abstract - Image processing has traditionally involved the use of square operators on regular rectangular image lattices. For many years the concept of using hexagonal pixels for image capture has been investigated, and several advantages of such an approach have been highlighted. We present a design procedure for hexagonal gradient operators, developed within the finite element framework, for use on hexagonal pixel based images. In order to evaluate the approach, we generate pseudo hexagonal images via resizing and resampling of rectangular images. This approach also allows us to present results visually without the use of hexagonal lattice capture or display hardware. We provide comparative results with existing gradient operators, both rectangular and hexagonal.

Keywords: hexagonal image processing; scalable operator; tri-directional operator; gradient operator

1. Introduction

In machine vision, feature detection is often used to extract salient information from images. Image content often represents curved structures, which increase the complexity of the information to be processed compared with structures that can be described by a discrete set of directions. Most well-known operators on a conventional rectangular lattice exhibit limitations when detecting curved edges, most commonly due to the processing being aligned principally in the horizontal and vertical directions. Potentially image information is excluded or lost due to failure to represent and process curves accurately [24]. One method to improve the treatment of curved objects

is the use of compass operators that rotate feature detection masks to successfully detect diagonal edges [19]. An alternative approach is to increase the image resolution if possible [15]. This can help to reduce the loss of information, but increase in image resolution generally leads to an increase in computational cost. To overcome this problem, an alternative sampling lattice, i.e., hexagonal, can be introduced.

Machine vision systems are often modelled on characteristics of the human vision system, in which photoreceptors in the human fovea are densely packed in an hexagonal structure as illustrated in Figure 1. The characteristics of the human vision system have been used to construct a noise spectrum [3] and, Gabor filters [31] for use on a hexagonal grid structure. Applications have been developed including biologically-inspired fovea modelling with neural networks that correspond to the hexagonal biological structure of photoreceptors [9], and silicon retinas for robot vision [17], [28]. Indeed, hexagonal lattices have been explored for approximately forty years [8], [33], [29]; research on processing hexagonal images includes areas such as image reconstruction [33], [13], hexagonal filter banks [11], blue-noise halftoning [9], and robot exploration [22].
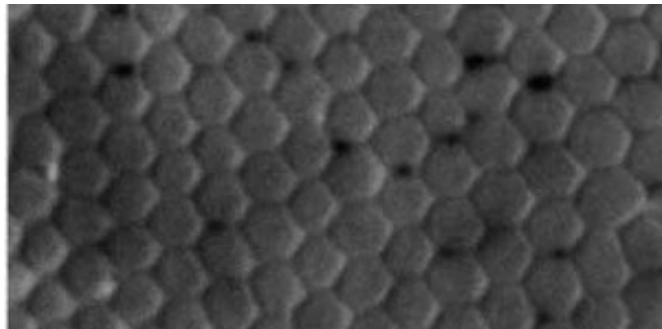

Figure 1: Cross section of human fovea showing the hexagonal structure of the photoreceptor

cones densely packed [5]

There is a number of fundamental advantages of using the hexagonal grid structure for digital image representation. One of the major advantages is the consistency available in terms of neighbouring pixel distances when tiling an image plane. In a rectangular grid, the distance d between neighbouring pixel centres depends on whether the neighbours are vertically/horizontally adjacent, (with d=1), or diagonally adjacent (with $d = \sqrt{2}$) as illustrated in Figure 2 (a).
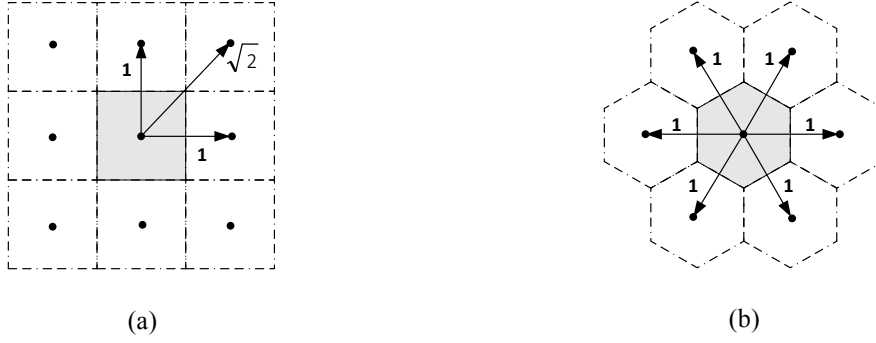
Figure 2. Adjacency properties of (a) a square lattice, (b) a hexagonal lattice

In a hexagonal lattice, the distances between all neighbouring pixels are equal, i.e., d=1 in all cases, as shown in Figure 2(b). This equidistance property facilitates the implementation of circular symmetric kernels and is associated with increased directional accuracy when detecting edges, both straight and curved [10]. The accuracy of circular and near circular operators for edge detection has been demonstrated in [27], [6]. Sampling on a hexagonal grid has also been shown to incur less aliasing [19] and greater efficiency in terms of sampling density than on a square lattice. Vitulli [23] shows that to achieve the same average vertical sampling density (i.e., the same number of pixel rows in the image) 13% fewer pixels are required with hexagonal sampling than with square sampling. Hence, less storage in memory will be needed for the image data, and potentially less computational time to process the image.

Many edge detection algorithms that exist for conventional images are based on components strongly aligned with the horizontal and vertical axes, and hence they are not readily adaptable to a hexagonal lattice. To date, only a small number of hexagonal gradient operators have been designed for use on hexagonal images, such as the work of Davies [6], Middleton [15], and Staunton [24]. More recently, Shima [30] designed new consistent gradient operators for direct use on hexagonal images; the approach is based on that in [25] where the operators are derived by minimizing the difference between the ideal gradient response and that obtained by the gradient operator. In addition, recent work has highlighted the advantages of omni-directional feature extraction [26], and in particular, Paplinski [1] has introduced tri-directional feature extraction on traditional rectangular pixel-based images. The use of a hexagonal image structure facilitates tri-directional feature extraction by introducing three natural axes along which directional derivative operators may be easily computed. One of the main advantages of using the three natural axes of symmetry is that directional derivatives along axial directions can be computed efficiently

by rotation. We need compute operators for only one specific axial direction (say, x-axis) and then transform the operator through 60° rotations to generate operators along the other two axial directions.

We present an efficient design procedure for the development of hexagonal tri-directional derivative operators that can be applied directly to hexagonal images. We show that only one operator (x-directional derivative) needs to be computed and the other two operators can then be obtained via appropriate rotation. We demonstrate that, unlike the approach of previously developed operators for use on hexagonal images, our design procedure facilitates the development of gradient operators of any size. For example, the operators developed by Davies [4], which use masks designed on the Cartesian axes, are not readily scalable to larger neighbourhood operators; the tri-directional hexagonal operators developed by Shima [18] use Fourier transforms, are quite computationally expensive and do not offer flexibility to readily scale the operator neighbourhood. In Section 3 we show our operator design procedure in detail, demonstrating that only a small number of simple function evaluations are required.

The paper is organised as follows: Section 2 describes the resampling technique that enables an image to be represented using hexagonal pixels. In Section 3 we present the tri-directional operator design, highlighting how this can be readily scalable to operators of any size. In Section 4 we present performance evaluation that illustrates that the proposed gradient operators are superior to the current state-of-the-art techniques when comparing performance over a range of edge orientations and displacements. Our approach, combined with the spatial sampling efficiency of a hexagonal structure, also provides improvements in computational performance in comparison with the use of traditional rectangular pixel-based images. A conclusion is provided in Section 5.

2. Resampling Techniques

One of the main restrictions on adoption of the hexagonal lattice for image representation and processing is the absence of availability of hardware: both sensors that enable the capture of hexagonal images and devices that enable their display. In order for research to advance in this area a resampling technique must be incorporated to enable the processing and display of hexagonal images using existing square lattice hardware.

In Gardiner et al. [7], a comparative evaluation was completed to determine the most appropriate resampling technique to generate hexagonal pixel-based images, evaluating those discussed in [34], [16], [21], [4]. Based on

the evaluation results obtained in [7], we have chosen to use the resampling technique in [4] throughout this work. Wuthrich [4] proposed a method of creating a pseudo hexagonal pixel, known as a hyperpel, from a cluster of square pixels. In [20], this approach is adapted to use sub-pixels to enable a hexagonal pixel to be formed from a cluster of square sub-pixels. Sub-pixel creation limits the loss of image resolution. As illustrated in Figure 3, each pixel of the original image is represented by a 7×7 pixel block of equal intensity in the new image [20]. This creates a resized image of the same resolution as the original image with the ability to display each pixel as a group of sub-pixels.
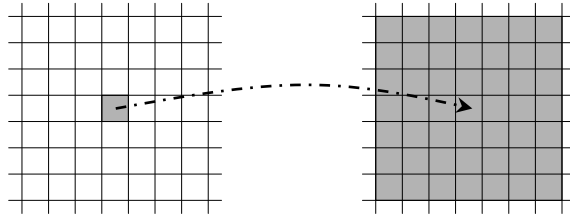

Figure 3. Resizing of a pixel to a 7×7 pixel block

The motivation for image resizing is to enable the display of sub-pixels, which is not otherwise possible. With this structure now in place, a cluster of sub-pixels in the new image, closely representing the shape of a hexagon, can be selected; this cluster represents a single hexagonal pixel in the resized image, and its intensity value is the average of the intensity values of its sub-pixels. Selection of the number of sub-pixels to be clustered for each hexagonal pixel is based on two issues: the arrangement must allow a tessellation of the image plane; and the cluster must closely resemble a hexagon in shape. Based on our evaluation in [7], we use the 56 sub-pixel cluster illustrated in Figure 4.
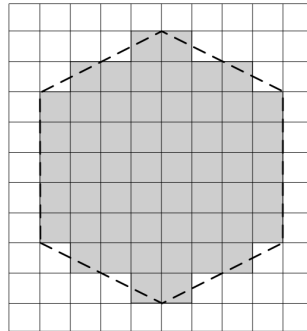

Figure 4. Sub pixel cluster representations of a hexagonal pixel

3. Scalable Tri-Directional Operator Design Framework

We present a design procedure for gradient operators that is developed within a finite element framework. By this we mean that a number of principles that underpin finite element computation are used to develop and implement the operators. Firstly, we establish a mesh of equilateral triangular elements based on the hexagonal pixel lattice. The image is then represented as a piecewise polynomial function (piecewise linear) over this computational mesh. To develop an operator that is implemented on a specific neighbourhood a test function is selected and used in a weak form of the operator. This involves numerical integration of the test function with the image derivative over the neighbourhood; operators at different scale can be achieved by selecting differently sized neighbourhoods and correspondingly scaled test functions. As in the finite element method, an operator is constructed by a process of element assembly. This means that a neighbourhood integral is computed by assembling a collection of element integrals corresponding to the triangular elements contained within the neighbourhood. Hence it is unnecessary to compute an entire operator all at once; rather, simple element integrals are computed in a systematic fashion and the element integrals are "assembled" using element-node relationships that are a standard part of the mesh description in the finite element method. Each element integral can be computed efficiently by low order integration (three function evaluations) as the test function is smooth on each element and each basis function is linear (and, therefore, its derivative constant). Coupled with the six-fold symmetry afforded by the computational mesh that is based on the hexagonal pixel lattice, this approach provides low computational complexity when scaling to larger operators.

The use of the finite element framework enables a unified approach to be taken to the design and implementation across different pixel lattices. In [17] we have used the finite element framework with a traditional rectangular pixel array to develop and analyse near-circular operators. When used with a hexagonal pixel array the six-fold symmetry of the naturally occurring computational grid of equilateral triangular elements enables particularly efficient implementation through use of rotational symmetries. This means that, unlike other hexagonal methods, not only are we able to provide a systematic technique for scaling operators on a hexagonal grid, we can do this with low computational complexity – even more so than on a rectangular grid, due to the increased degree of rotational symmetry present in the computational mesh.

3.1 Hexagonal image representation

With reference to the resized hexagonal image, it is possible to represent this image by an array of samples of a continuous function $u(x, y)$ of image intensity on a domain Ω. Figure 5 shows a selection of hexagonal pixels with nodes placed at the centre of each pixel. These nodes are the reference points for computation based on finite element techniques to be used throughout the domain Ω.
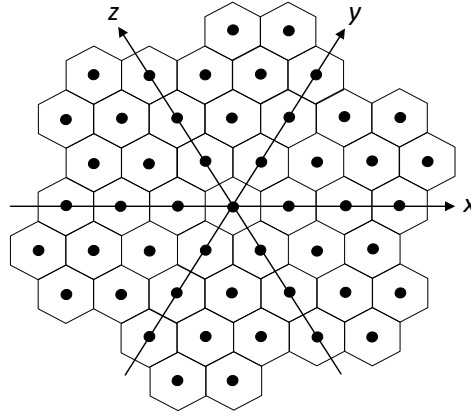
Figure 5. Axes directions in a hexagonal image

3.2 Operator design

We propose operators for use on a hexagonal pixel-based image with structure as illustrated in Figure 5. The scalable operator design procedure is based on the use of a "virtual mesh" consisting of equilateral triangular elements and which overlays the hexagonal pixel array as shown in Figure 6.
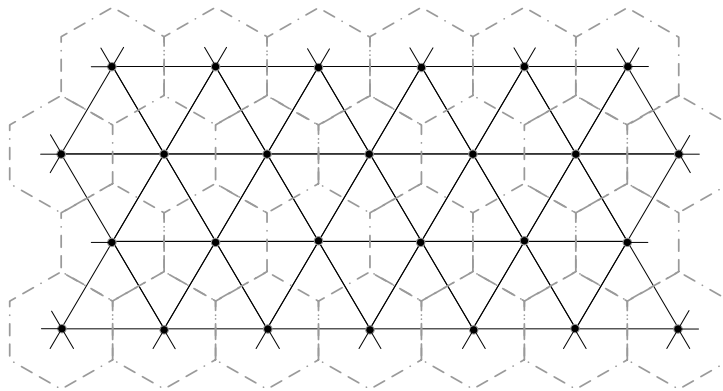
Figure 6. Virtual mesh of equilateral triangular elements

Typically image processing gradient operators are based on the construction of two independent directional derivative operators aligned in the horizontal and vertical directions. Here we present a computationally efficient approach to hexagonal image processing operator implementation by designing a tri-directional operator, i.e., three hexagonal operators that are aligned along the x-, y- and z- hexagonal axes illustrated in Figure 5. Computation is efficient as only one operator needs to be computed: say, the x- directional operator. This operator can then be rotated by $60°$ and $120°$ to obtain the y- and z- directional derivative operators respectively.

Redundancy exists between the three operator masks of a tri-directional operator, allowing, for example, the x-directional operator mask to be computed as a combination of the other two operator masks using the relationship $y = x + z$. This is not considered to be a major weakness of the operator design as this relationship facilitates the implementation of Cartesian axes operators if required by appropriate combination of the tri-directional masks. It should be noted that, although the hexagonal structure naturally contains three axes, we use only two axes in the co-ordinate system in order to ensure a unique representation. Hence, we have chosen to work with the x- and y-axes shown in Figure 7.
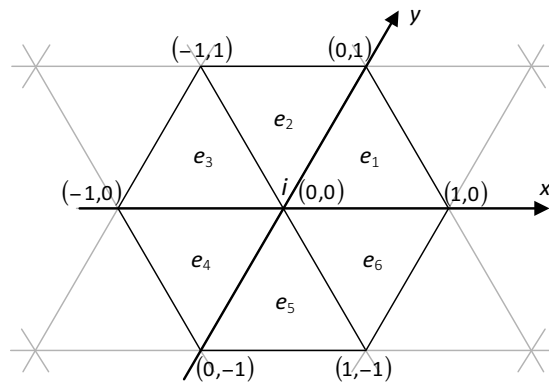

Figure 7. Hexagonal co-ordinate system

For the derivation of the primary operator, the x-directional operator, with any node (x_i, y_i) we associate a piecewise linear basis function which has the properties

$$\phi_i(x_j, y_j) = \begin{cases} 1 & \text{if } i = j \\ 0 & \text{if } i \neq j \end{cases}$$

(1)

$\phi_i(x, y)$ is thus a "tent-shaped" function with support restricted to a small neighbourhood centred on node (x_i, y_i) consisting of only those elements that have node (x_i, y_i) as a vertex. Then we may approximately represent the image u over a neighbourhood Ω_i^σ centred on node i by a function

$$U(x, y) = \sum_{j \in D_i^\sigma} U_j \phi_j(x, y)$$

(2)

in which the parameters $\{U_j\}$ are the sampled image intensity values and D_i^σ is the set of nodes contained in Ω_i^σ. Hence we obtain a piecewise linear representation of the image on the neighbourhood Ω_i^σ, where the parameter σ is representative of the neighbourhood size.

As we are concerned initially with the development of only a x-directional derivative operator, a weak form is obtained by considering only the x derivative term, multiplying it by a test function $v \in H^1$, and integrating over the image domain Ω to give

$$E(u) = \int_\Omega \frac{\partial u}{\partial x} v \, d\omega$$

(3)

In the finite element method a finite-dimensional subspace $S^h \subset H^1$ is used for function approximation. Our design procedure also incorporates a finite-dimensional test space $T_\sigma^h \subset H^1$ that explicitly embodies a scale parameter σ, enabling the development of adaptive derivative operators. Hence, we use a test function ψ_i^σ that is restricted to have support over an operator neighbourhood Ω_i^σ. Operator neighbourhoods for the first three operator sizes (7-, 19-, 37-nodes) are shown in Figure 8. The test function is then used in the weak form of the first derivative operator, providing the functional

$$E_i^\sigma(U) = \int_{\Omega_i^\sigma} \frac{\partial U}{\partial x} \psi_i^\sigma \, d\omega_i$$

(4)

In the following Section 3.3 we start by explaining the operator imlementation process in the case of the smallest (7-node) operator. We then explain how implementation is extended to larger operators and how rotational symmetries are exploited to maintain low computational complexity.
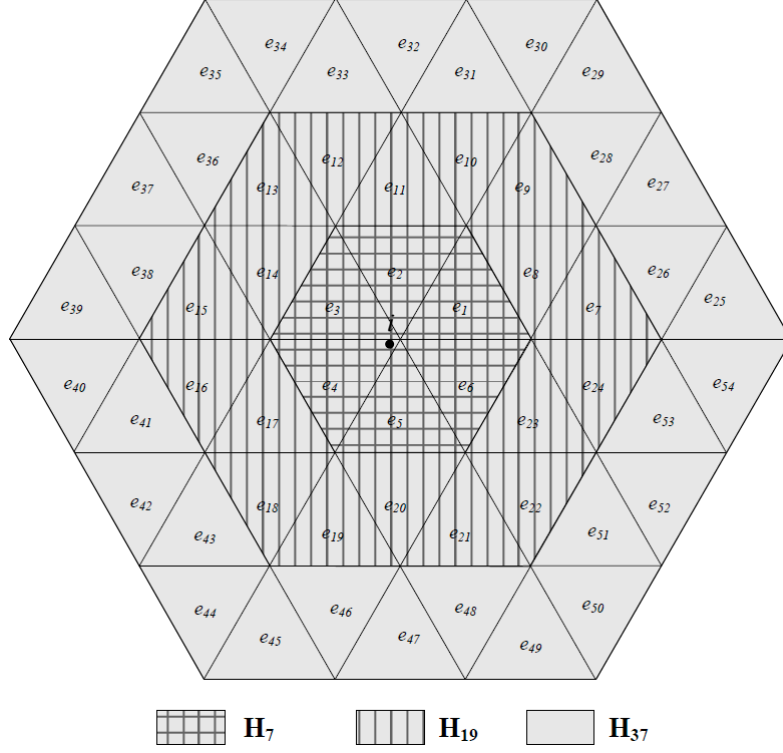
Figure 8. Hexagonal operator neighbourhoods for operator sizes H_7, H_{19} and H_{37}

3.3 Operator Implementation

To illustrate the implementation of the primary 7-point first order hexagonal operator, consider the H_7 hexagonal structure in Figure 8. Here the smallest neighbourhood centred on node i covers a set of six elements $\{e_m\}$. The test function ψ_i^σ associated with the central node i shares common support with ϕ_i and the surrounding six basis functions $\{\phi_k\}$. Hence $E_i^\sigma(U)$ can be computed over the six elements in the neighbourhood Ω_i^σ by substituting the image representation (equation 2) into the functional $E_i^\sigma(U)$, which yields

$$E_i^\sigma(U) = \sum_{j=1}^{N} K_{ij}^\sigma U_j$$

(5)

where

$$K_{ij}^\sigma = \sum_{m|e_m \subset \Omega_i^\sigma} k_{ij}^{m,\sigma}$$

(6)

and $k_{ij}^{m,\sigma}$ is the element integral

$$k_{ij}^{m,\sigma} = \int_{e_m} \frac{\partial \phi_j}{\partial x} \psi_i^\sigma \, d\omega \tag{7}$$

computed over element $e_m \subset \Omega_i^\sigma$. The test functions ψ_i^σ used in this operator design are a set of Gaussian basis functions expressed as

$$\psi_i^\sigma = \frac{1}{2\pi\sigma^2} e^{\left(-\frac{\left(x + \frac{1}{2}y \right)^2 + \left(\frac{\sqrt{3}}{2}y \right)^2}{2\sigma^2} \right)} \tag{8}$$

and restricted to the operator neighbourhood Ω_i^σ. The test function builds in smoothing to the operator design, removing the necessity for any image pre-processing. The value of σ is determined as $W/1.96$, where W is the operator width; this ensures that 95% of the central cross-section of the Gaussian function falls within the operator neighbourhood.
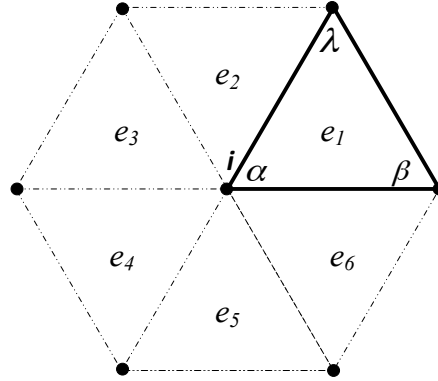

Figure 9. Six elements centred at node i of a neighbourhood Ω_i^σ

For each of the six triangular elements within the neighbourhood, a triangular element operator must be generated whose entries map directly to the corresponding spatial locations within the 7-point operator neighbourhood. To illustrate this, consider element e_1 shown in Figure 9. The Gaussian test function ψ_i^σ shares common support with the linear basis functions ϕ_j, where $j = \alpha, \beta, \lambda$ and thus the first derivative triangular element operator is computed as

$$K_i^{1,\sigma} = \begin{bmatrix} & k_{i,\lambda}^{1,\sigma} & \\ k_{i,\alpha}^{1,\sigma} & & k_{i,\beta}^{1,\sigma} \end{bmatrix} \tag{9}$$

Using a two co-ordinate system whose origin is at node i as in Figure 7, $k_{ij}^{1,\sigma}$ is computed as

$$k_{i\alpha}^{1,\sigma} = \int_0^1 \int_0^{1-x} \frac{\partial \phi_j}{\partial x} \psi_i^{\sigma} |J| dx dy$$

(10)

for $j = \alpha, \beta, \lambda$. With nodal separation normalised to unity as in Figure 7, the Jacobian J has a value of $\sqrt{3}/2$.

Using the coordinate system with origin at node i, the basis functions ϕ_j can be defined on element e_1 as

$$\phi_\alpha = 1 - x - y, \qquad \phi_\beta = x \quad \text{and} \qquad \phi_\lambda = y$$

(11)

and when differentiated with respect to x we obtain

$$\frac{\partial \phi_\alpha}{\partial x} = -1 \qquad \frac{\partial \phi_\beta}{\partial x} = 1 \quad \text{and} \qquad \frac{\partial \phi_\lambda}{\partial x} = 0$$

(12)

To illustrate element operator computation, consider nodes α, β and λ in e_1. Then $k_{i\alpha}^{1,\sigma}$ may be written as

$$k_{i\alpha}^{1,\sigma} = \int_0^1 \int_0^{1-x} (-1) \frac{1}{2\pi\sigma^2} e^{-\left(\frac{\left(x + \frac{1}{2}(y)\right)^2 + \left(\frac{\sqrt{3}}{2}(y)\right)^2}{2\sigma^2} \right)} \cdot \frac{\sqrt{3}}{2} dx dy$$

(13)

$k_{i\beta}^{1,\sigma}$ may be written as

$$k_{i\beta}^{1,\sigma} = \int_0^1 \int_0^{1-x} (1) \frac{1}{2\pi\sigma^2} e^{-\left(\frac{\left(x + \frac{1}{2}(y)\right)^2 + \left(\frac{\sqrt{3}}{2}(y)\right)^2}{2\sigma^2} \right)} \cdot \frac{\sqrt{3}}{2} dx dy = -k_{i\alpha}^{1,\sigma}$$

(14)

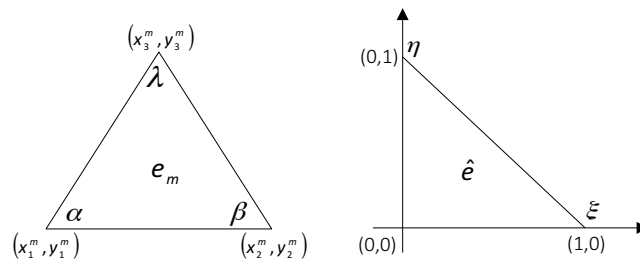and $k_{i\lambda}^{1,\sigma} = 0$.

Figure 10. Local co-ordinate reference for equilateral triangle

As computation of each element integral $k_{ij}^{m,\sigma}$ involves evaluation of a Gaussian function, numerical integration is used to approximate the integrals. In order to achieve this in a systematic manner, a local co-ordinate reference system for a right-angled triangle is introduced as illustrated in Figure 10, with co-ordinates ξ and η such that $\xi \geq 0$, $\eta \geq 0$ and $1 - \xi - \eta \geq 0$. A transformation maps the hexagonal coordinate system used for each element to a Cartesian coordinate system in order to enable use of a standard two-dimensional Gauss-Legendre integration rule. Mappings from e_m to $\hat{e}$ are defined by

$$x = (x_2^m - x_1^m)\xi_i + (x_3^m - x_1^m)\eta_i + x_1^m \tag{15}$$

$$y = (y_2^m - y_1^m)\xi_i + (y_3^m - y_1^m)\eta_i + y_1^m \tag{16}$$

Since ϕ_j is linear on each element, and ψ_i^σ is smooth, sufficient accuracy and computational parsimony can be achieved by using just three integration points in each element (which correspond, after mapping, to three standard Gauss- Legendre integration points in the standard right-angled triangle). Hence to compute each value k in each triangular element operator K in equation (9) requires only three evaluations of a Gaussian function; so 9 such function evaluations are required to compute K. Due to the six-fold reflectional symmetry of the six element neighbourhood shown in Figure 9, only two element matrices, K, have to be computed in order to determine the complete operator shown in equation (17). The computational complexity of the design approach is therefore low, as only a maximum of 18 Gaussian function evaluations are required to compute the operator.

On completion of each element operator, the 7-point mask is constructed by finite element assembly. This 7-point operator computes the local gradient along the x-direction and has the structure shown in equation (17). The operator is denoted by H_7^x, and the values of the co-efficients a and b are 0.147 and 0.295, respectively.

$$H_7^x = \begin{bmatrix} & -a & & +a & \\ -b & & 0 & & +b \\ & -a & & +a & \end{bmatrix} \tag{17}$$

13

By rotating the *x*-directional operator anti-clockwise by 60° and 120°, the *y*- and *z*- directional operators can be readily obtained, respectively, as

$$\mathrm{H}_7^y = \begin{bmatrix} & +a & +b \\ -a & 0 & +a \\ & -b & -a \end{bmatrix} \quad \mathrm{H}_7^z = \begin{bmatrix} & +b & +a \\ +a & 0 & -a \\ & -a & -b \end{bmatrix} \tag{18}$$

When calculating the gradient response for tri-directional derivative operators, redundancy is introduced due to the relationships by rotation between the three operators, and the gradient magnitude can be represented using only operators H_n^x and H_n^z as

$$|G_n| = \frac{2}{\sqrt{3}} \sqrt{(H_n^x)^2 + (H_n^z)^2 + H_n^x . H_n^z} \tag{19}$$

To extend the operator implementation to larger scales we consider how rotational symmetries may be used to achieve computational efficiency. For the smallest operator H_7^x developed above, it was necessary to compute element integrals over only element e_1 in Figure 7, and, since the basis functions are linear, only a single value, $k_{i\alpha}^{1,\sigma}$, was required. Then $k_{i\beta}^{1,\sigma} = -k_{i\alpha}^{1,\sigma}$, and $k_{i\lambda}^{1,\sigma} = 0$. Since the test function ψ_i^{σ} has infinite rotational symmetry, element integrals over the other five elements $e_2, e_3, e_4, e_5, e_6 \subset \Omega_i^{\sigma}$ $e_2, e_3, e_4, e_5, e_6 \subset \Omega_i^{\sigma}$ may be obtained as $\pm k_{i\alpha}^{1,\sigma}$ or 0 by making use of rotational symmetries. The entire operator H_7^x may then be constructed efficiently through finite element assembly. This approach is readily extended to larger operators. For the next operator H_{19}^x, we need consider only the extension of the sector containing element e_1, i.e., one-sixth of the neighbourhood, comprising elements e_1, e_7, e_8 and e_9 in Figure 7. Within this sector, from rotational symmetry it can be seen that element integrals computed over e_7 will be the same as those computed over e_7, and so element integrals are required over only two new elements: e_7 and e_8. Element integrals over the other five sectors of the neighbourhood for H_{19}^x are then obtained through rotational symmetries, enabling H_{19}^x to be constructed by finite element assembly after computing element integrals on only two new elements. Similarly, for H_{37}^x we need consider only extension of the sector to include new elements $e_{25}, e_{26}, e_{27}, e_{28}$ and e_{29}. Here, element integrals computed over e_{25} and e_{29}, and over e_{26} and e_{28}, will be the same, respectively. Hence element integrals are required over only three new elements: e_{25}, e_{26} e_{25}, e_{25} and e_{27}. In general, it is straightforward to establish that the computational complexity of extending the scale of the operator is linear in terms of the number of new elements over which element integrals need to be computed. Since computation of any element integral requires

just three function evaluations of the test function, computational complexity is therefore simply linear in function evaluations as the operator scale is increased.

4. Performance Evaluation

Evaluation is presented to compare the performance of our proposed approach of scalable hexagonal tri-directional operators with other existing derivative operators that can be applied directly to hexagonal images and with equivalently sized square operators for use on standard rectangular lattice images. Hexagonal operators used for comparison in this evaluation include the modified Sobel [15] and modified Prewitt [24] hexagonal operators, the Davies hexagonal operator [6], and the Shima hexagonal operator [30]. It should be noted that hexagonal Sobel, Prewitt and Davies operators exist only at one scale, namely the scale associated with the smallest proposed operator size, H_7, whereas the Shima operator has been developed using two neighbourhood operator sizes, 7-point and 19-point.

One advantage of hexagonal operators is their directional anisotropy due to the equidistant neighbourhood pixel separation. Because of this directional anisotropy, we can consider hexagonal operators to be near-circular operators, and, therefore, to conduct a fair comparison with square operators, we compare our set of proposed hexagonal operators with the finite element based near-circular operators developed for use on square pixel-based images in [2]. Such operators have already demonstrated improved angular accuracy for edge detection compared with similar square operators on a rectangular lattice.

To implement and evaluate our proposed operators using hexagonal pixel-based images we create a virtual hexagonal environment that simulates the use of a hexagonal image sensor. We initially create hexagonal pixel-based images, as described in Section 2, and then process the images using the operators described in Section 3 and the comparators listed above (modified Sobel, modified Prewitt, Davies and Shima). Evaluation of operator performances takes place within the virtual hexagonal environment. To assess the performance of our proposed operators, evaluation is conducted on both synthetic image data and real image data. In Section 4.1, two evaluation approaches are applied to synthetic data: Figure of Merit [32], comparing the operator's edge response with the expected edge response with respect to edge location; and Edge Sensitivity Analysis [14], comparing the accuracy of the operator's response with respect to magnitude, strength and edge displacement. In Section 4.2, evaluation on real image data is conducted using the Robust Visual Method [18], an evaluation technique that provides a

measure of performance based on a visual rating score. Using these three measures of operator evaluation provides a strong evaluation framework to fairly compare our proposed hexagonal derivative operators with existing operators.

4.1 Synthetic Image Data Evaluation

The first evaluation approach presented is the Figure of Merit. In order to accurately measure the performance of hexagonal gradient operators, we have modified the well-known Figure of Merit technique to accommodate the use of hexagonal pixel-based images. This technique considers three major areas of error associated with the determination of an edge: missing valid edge points; failure to localise edge points; classification of noise fluctuations as edge points. In addition to these considerations, when measuring edge detection performance, edge detectors that produce smeared edge locations should be penalised, whilst those that produce edge locations that are localised should be awarded credit. Hence Pratt introduced the Figure of Merit technique as one that balances the three types of error above, defined as

$$R = \frac{1}{\max{(I_A, I_I)}} \sum_{i=1}^{I_A} \left(\frac{1}{1 + \alpha d^2} \right) \tag{19}$$

where I_A is the actual number of edge pixels detected, I_I is the ideal number of edge pixels, d is the separation distance of a detected edge point normal to a line of ideal edge points, and α is a scaling factor. The Figure of Merit is normalised such that R takes values between 0 and 1, where 1 represents a perfectly detected edge. The scaling factor, α, is most commonly chosen to be 1/9, although this value may be adjusted to penalise edges that are localised but offset from the true edge position. Since knowledge of the actual edge location is necessary, this method can only be used on synthetic images.

To provide a realistic environment to compare operator responses, the Figure of Merit (FoM) technique is used on images with varying signal-to-noise ratios (*SNR*), where $\text{SNR} = h^2/\sigma_n^2$, h is the height of the step edge and σ_n^2 is the variance of the noise. Synthetic images for Figure of Merit measurements typically contain horizontal, vertical or oriented edges. However, one proposed advantage of hexagonal pixel-based images is their ability to accurately represent curves in real images. Therefore, we extend the standard use of the Figure of Merit technique to incorporate the measure of detected curved edges. The synthetic test images used for evaluation are generated using h=58 with SNR = 100, 50, 20, 10, 5 and 1 and contain a horizontal edge, an edge oriented at 60° or a curved edge (examples of which are presented in Figure 11). Five sets of test images were generated for each edge type,

at each SNR (totalling 90 test images). The FoM was calculated for each operator over the test image set and averaged to obtain an accurate Figure of Merit result.

(a) Horizontal edge (SNR=1) (b) 60° oriented edge (SNR=10) (c) Curved Edge (SNR=100)
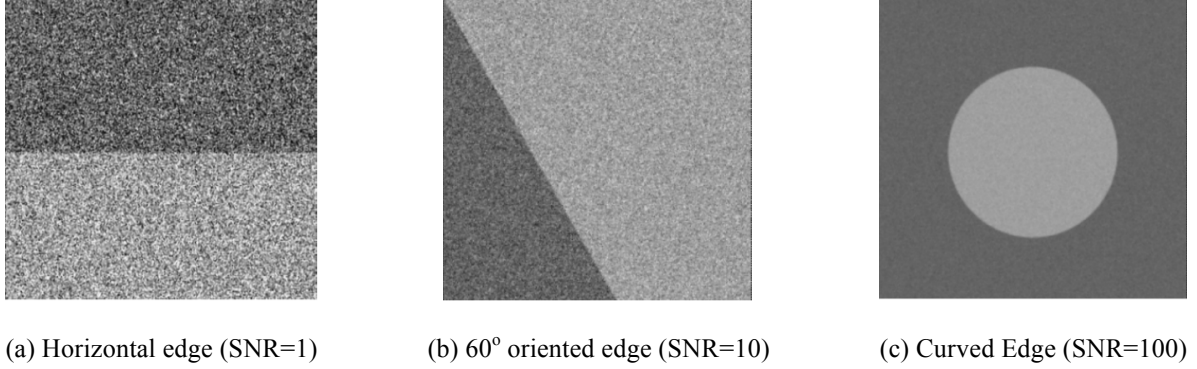
Figure 11. Example images for use in Figure of Merit

The results shown in Figure 12 indicate that the accuracy of the proposed H_7 tri-directional operator is greater than that of the Prewitt operator in all evaluated edge directions, and the same as obtained by the Sobel and Davies operators. This is due to the Sobel and Davies operators being equivalent to the proposed operator H_7 in relation to their weight proportions, i.e. the weight values of the operators are proportioned to achieve smoothing by giving greater importance to the centre weight values.

As our proposed operator is readily scalable to any operator size, we also compare the operator performance with the Shima operator, the only existing hexagonal operator that can accommodate a neighbourhood exceeding seven pixels in size. The Shima operator has been developed using two neighbourhood operator sizes, 7-point and 19-point (denoted as Shima7 and Shima19 respectively), and so these are compared with our H_7, H_{19} and H_{37} tri-directional operators. The Figure of Merit results are presented in Figure 13(a)–(c), which demonstrates that although our proposed 7-point hexagonal operator (H_7) performs equivalently to the 7-point Shima operator, the larger scale operators (H_{19} and H_{37}) perform significantly better than both the 7-point and 19-point Shima operators, particularly on images with high levels of noise.

To further evaluate the accuracy of our scalable tri-directional operators, we compute Figure of Merit results to compare the performance of the proposed operators applied directly to hexagonal images with the performance of equivalently sized square operators for use on standard rectangular lattice images. Again, three hexagonal operator sizes are used for evaluation with three equivalent near-circular operators, namely 3x3, 5x5 and 7x7, denoted by NC_{3x3}, NC_{5x5} and NC_{7x7} respectively. The results in Figure 13(d)-(f) show that, in most cases, the
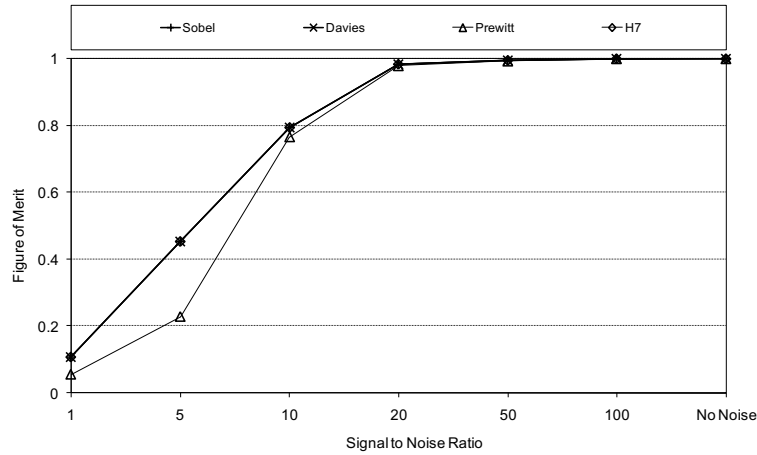
proposed hexagonal operators detect edges more accurately than the equivalent near-circular operators applied to square images, particularly in images with high levels of noise.
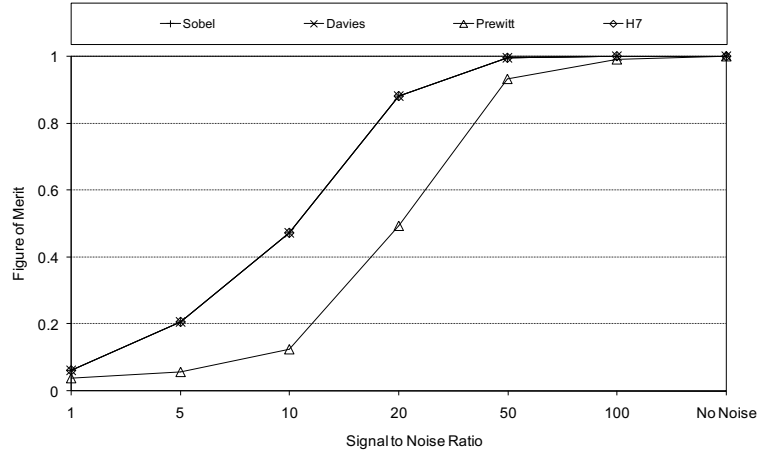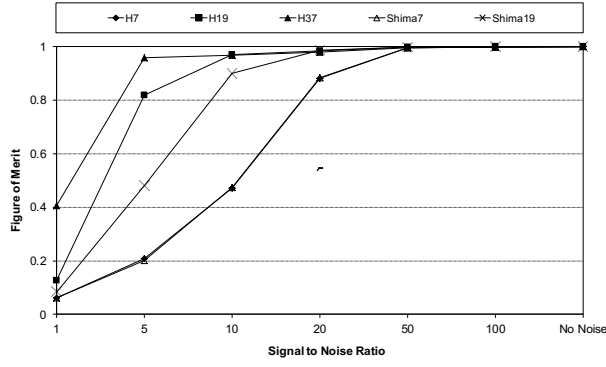

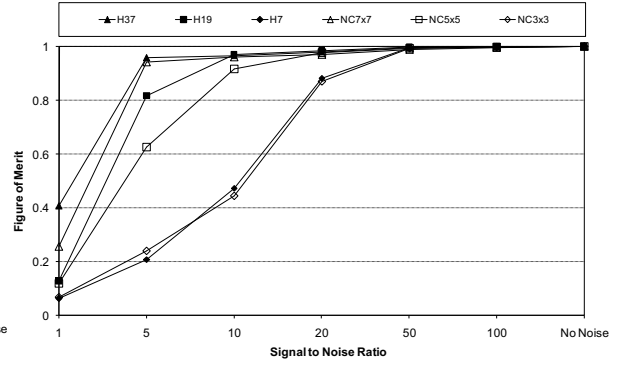(a) FoM computed on a horizontal edge
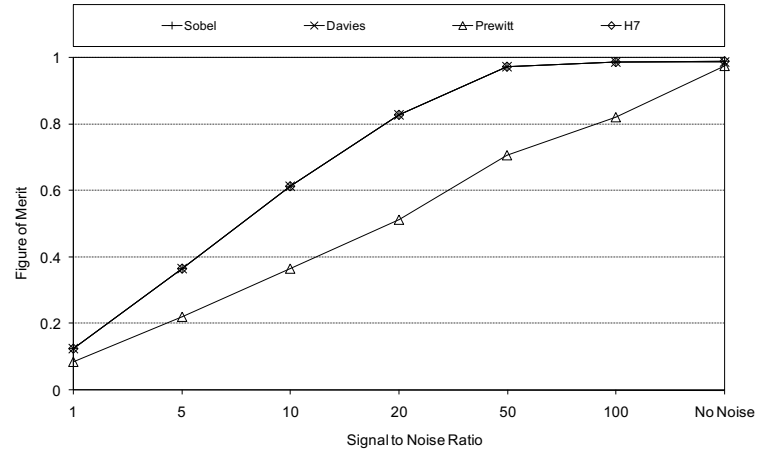
(b) FoM computed on a curved edge
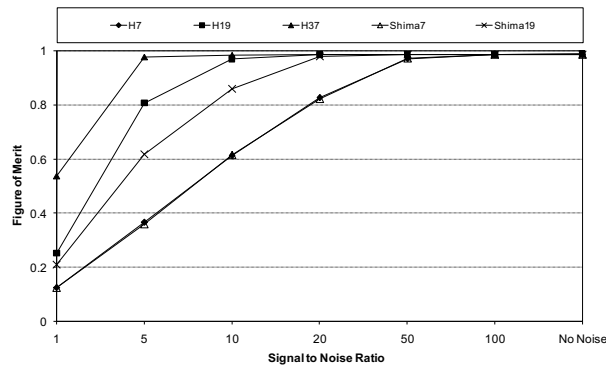

(c) FoM computed on an oriented edge 60°

Figure 12: Figure of Merit results to compare tri-directional operator with existing 7-point hexagonal operators
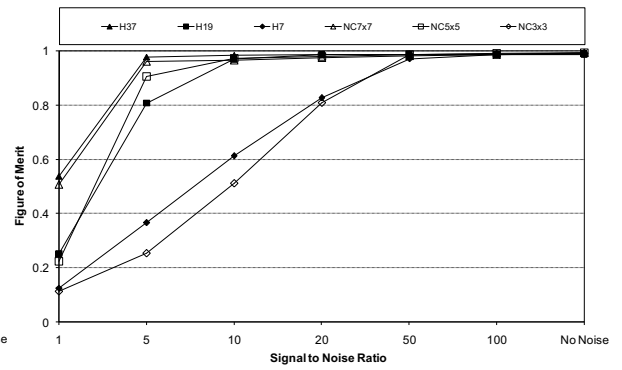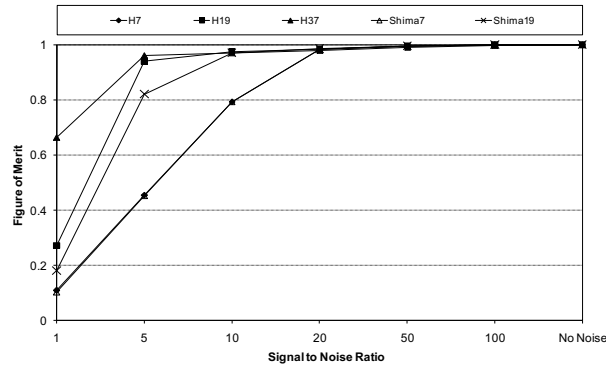
(a) FoM computed on a horizontal edge
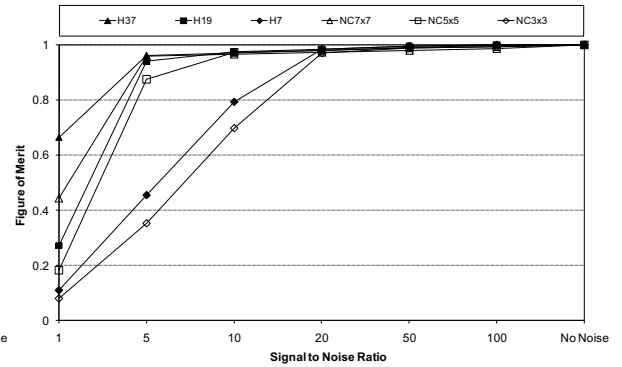
(d) FoM computed on a horizontal edge

(b) FoM computed on a curved edge

(e) FoM computed on a curved edge

(c) FoM computed on an oriented edge 60°

(f) FoM computed on an oriented edge 60°

Figure 13: Figure of Merit results to compare tri-directional operators with: (a)-(c) Shima operators

(hexagonal pixel based operators); (d) – (f) circular operators of equivalent sizes

For the larger scale operator H_{37} we also provide comparative performance evaluation with Marr-Hildreth and the SUSAN operator of similar size. In Figure 14(a) and Figure 14(b) we see that Figure of Merit values are substantially better for H_{37} than for Marr-Hildreth or SUSAN for low signal-to-noise ratios.
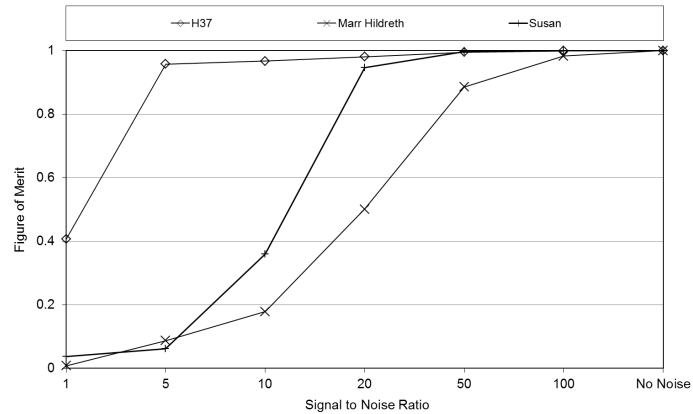
(a) FoM computed on a horizontal edge
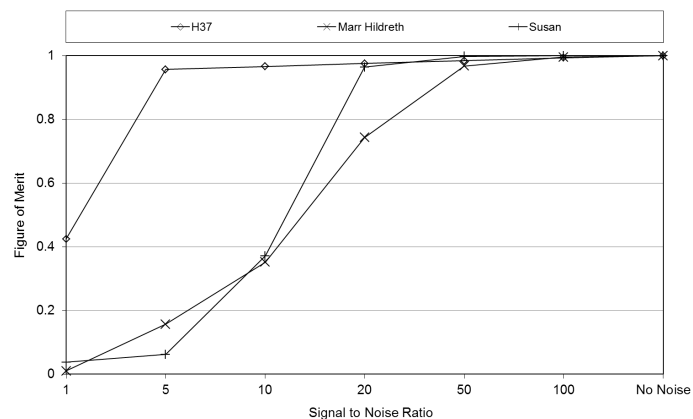
(b) FoM computed on a vertical edge

Figure 14: Figure of Merit results to compare tri-directional operators with Marr-Hildreth Laplacian of Gaussian and the SUSAN operator

The second performance evaluation approach, edge sensitivity analysis [14], is presented in Figure 16, Figure 17 and Figure 18. This approach enables comparison of operator performance over a range of edge orientations and displacements. The edge model takes into consideration the edge orientation and the displacement of the edge from the centre point of the edge model. These can be measured by creating an edge model of an infinite straight step edge with unit intensity on one side and zero intensity on the other, allowing the edge to be characterised by the straight line defining the boundary. The line is parameterised with respect to its orientation from the origin, θ, and the line's displacement from the origin, ρ, see Figure 15.

This edge sensitivity model has been designed for use on a conventional rectangular lattice, but we have extended the model for use on the hexagonal lattice. Kitchen and Malin's edge model is used to create an infinite horizontal straight step edge where both θ and ρ can be incremented simultaneously. The pixel intensities at each increment can be directly resampled to a hexagonal pixel-based image, where a hexagonally structured operator can be applied directly to the edge sensitivity model. Hexagonal operators can then be assessed directly using the images generated by the edge sensitivity evaluation technique in order to evaluate the sensitivity of an operator's response with respect to edge orientation and displacement. This adaptation allows the sensitivity of both rectangular and hexagonal operators to be compared fairly on a common framework.
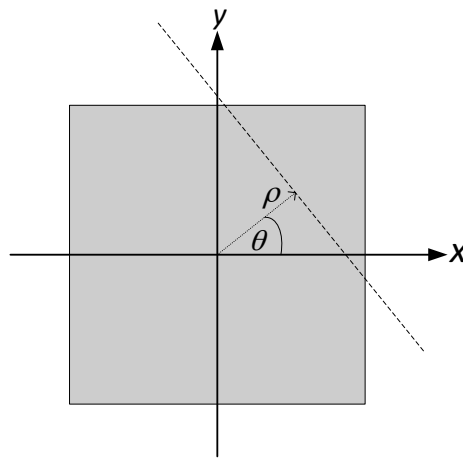

Figure 15. Parameters of edge sensitivity model

An ideal result is represented by the horizontal dashed lines at each orientation in the edge sensitivity graphs. In Figure 16 the response from the proposed 7-point tri-directional operator is compared with the hexagonal Prewitt operator and the equivalently sized square neighbourhood operator (NC_{3x3}). Due to the equivalence of the Sobel, Davies and $Shima_7$ operators with the proposed H_7 operator, the edge sensitivity analysis for these operators is not shown. Results show that the H_7 tri-directional operator provides similar performance to the Prewitt operator, with the performance of the NC_{3x3} operator being slightly superior. However, results for larger neighbourhood operators shown in Figure 17 and Figure 18 demonstrate how the performance accuracy of the proposed tri-directional operator increases as the operator size increases (H_{19} and H_{37}), providing improved performance over existing hexagonal and square neighbourhood operators. This is clearly shown by the edge sensitivity error tables Table 1, Table 2 and Table 3, where the average error for each angle is compared across operators of equivalent size. Table 1 compares the average error for operators equivalent in size to the proposed H_7 operator; Table 2 compares operators equivalent in size to H_{19}, and Table 3 compares operators equivalent in size to H_{37}.
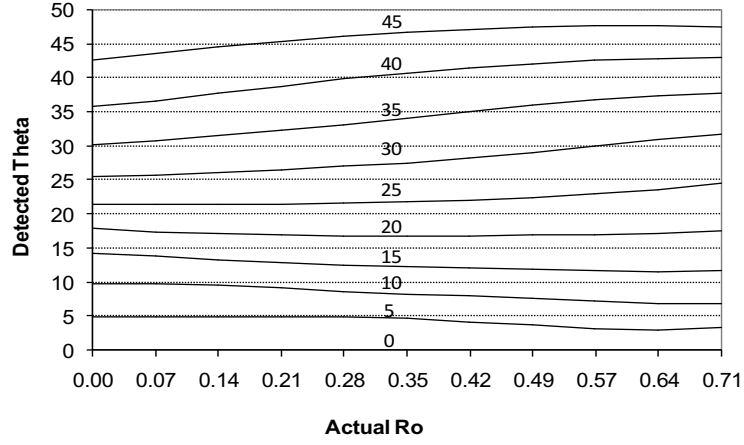
(a) Edge sensitivity results for Prewitt hexagonal operator
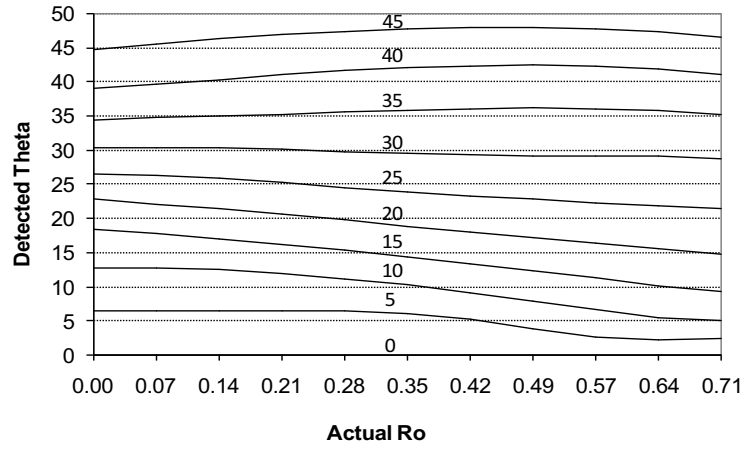
(b) Edge sensitivity results for H$_7$ hexagonal operator
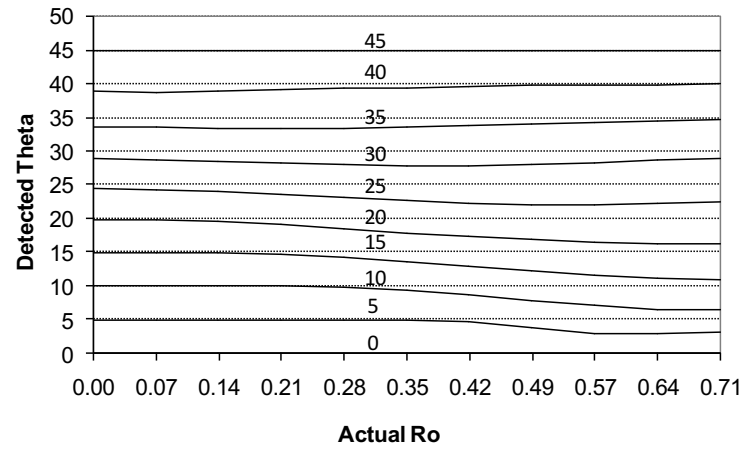
(c) Edge sensitivity results for NC$_{3x3}$ square operator

Figure 16: Edge sensitivity results comparing square and hexagonal operator responses

(a) Edge sensitivity results for Shima$_{19}$ operator
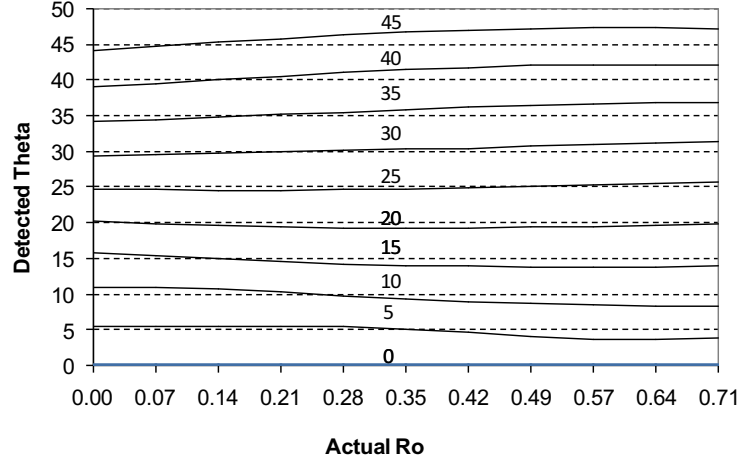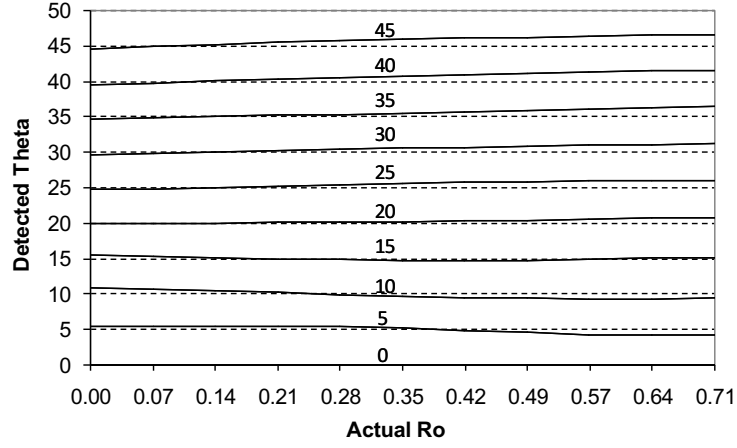

(b) Edge sensitivity results for H$_{19}$ operator
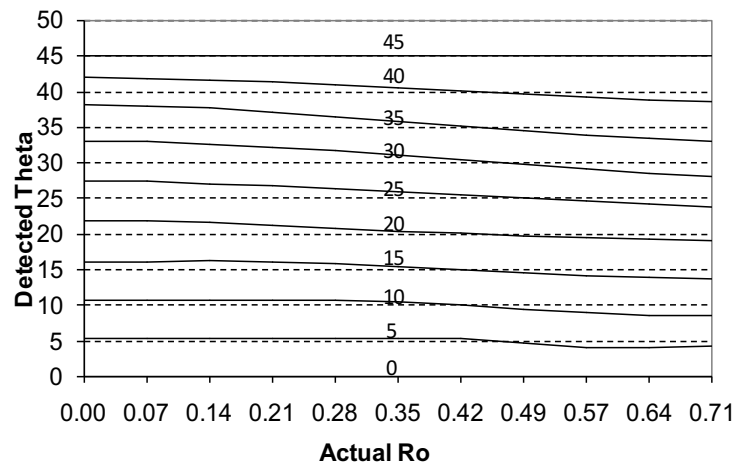
(c) Edge sensitivity results for NC$_{5x5}$ operator

Figure 17: Edge sensitivity results comparing square and hexagonal operator responses
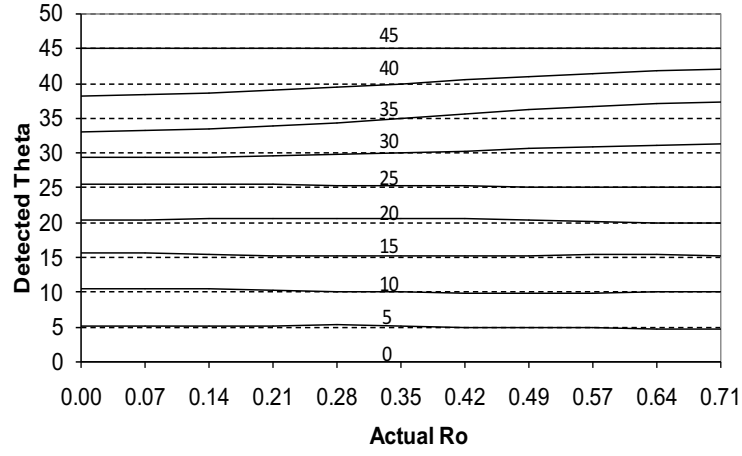
(a) Edge sensitivity results for NC$_{7x7}$ operator
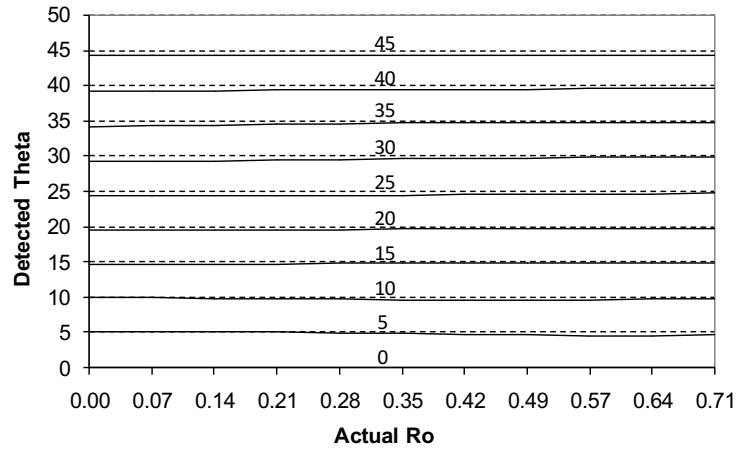
(b) Edge sensitivity results for H$_{37}$ hexagonal operator

Figure 18: Edge sensitivity results comparing square and hexagonal operator responses

Angle	Prewitt	NC$_{3x3}$	H$_7$
0°	0	0	0
5°	1.496	0.634	1.582
10°	2.861	1.187	2.482
15°	3.950	1.628	2.660
20°	4.623	1.925	2.388
25°	4.758	1.965	1.715
30°	4.469	1.653	0.585
35°	3.566	1.144	0.596
40°	2.045	0.577	1.459
45°	0	0	1.932

Table 1: Edge sensitivity errors for 7-point operators

Angle	Shima$_{19}$	NC$_{5x5}$	H$_{19}$
0°	0	0	0
5°	0.679	0.484	0.477
10°	0.979	0.762	0.520
15°	0.814	0.850	0.209
20°	0.416	0.850	0.295
25°	0.318	1.162	0.523
30°	0.605	1.564	0.565
35°	1.011	1.605	0.623
40°	1.369	1.054	0.793
45°	1.491	0	0.851

Table 2: Edge sensitivity errors for 19-point operator

Angle	NC$_{7x7}$	H$_{37}$
0°	0	0
5°	0.189	0.185
10°	0.180	0.233
15°	0.250	0.238
20°	0.358	0.362
25°	0.221	0.496
30°	0.575	0.446
35°	1.365	0.448
40°	1.217	0.641
45°	0	0.837

Table 3: Edge sensitivity errors for 37-point operator

4.2 Real Image Data Evaluation

In support of these observations, a qualitative method of evaluation using real images, the robust visual method, is used to further compare the performance of the proposed hexagonal operator with existing approaches. The Robust Visual Method is used to visually evaluate operator edge maps, based on human evaluators rating the visual integrity of edge maps generated by different operators. Most methods of evaluating operator output responses rely on the use of ground truth, but creating ground truth for real images can be time consuming and inaccurate. An advantage of the robust visual evaluation method is that it uses real images that rely on the subjective evaluation of edge maps by the human visual system and therefore does not require the use of ground truth. The real images used are selected such that they have a centrally placed object in the image foreground (Figure 19).

(a)   (b)   (c)   (d)

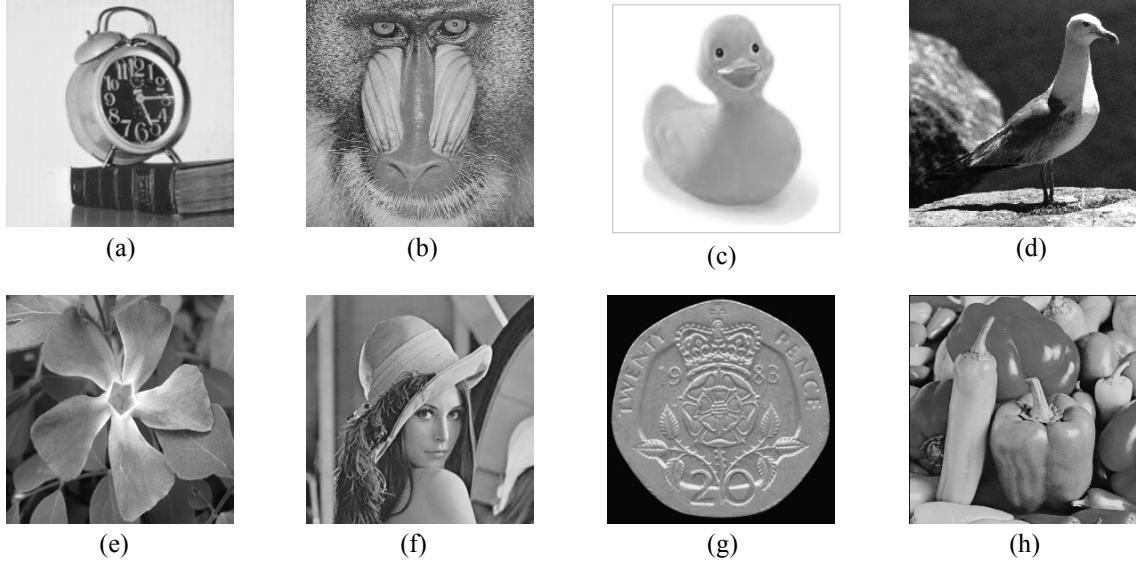(e)   (f)   (g)   (h)

Figure 19. Image set for Robust Visual Method of evaluation

In the robust visual method, the subjects rank each edge image on a scale of 1 to 7 according to how well they can recognise the centrally placed object, where 7 indicates easy recognition and 1 indicates no coherent information. The Intraclass Correlation Coefficient, calculated by the statistical measure $\text{ICC}(3,\text{k}) = \frac{\text{BMS}-\text{EMS}}{\text{BMS}}$ was used to ensure image rating consistency within the set of human subjects, where *BMS* is the mean square value of the rating, *EMS* is the total mean square error and *k* is the number of evaluators. In phase 1 of the technique, for any one image the human subjects rate six edge images generated by an operator over a range of thresholds. This results in the visually best edge map corresponding to each image for each operator being selected by the evaluators. In phase 2, the human subjects then rated the selected edge maps for each image on a scale of 1 to 7 in order to compare the overall performance of different operators. Again consistency was checked using *ICC*(3,*k*). Initially edge maps were generated for each of the eight images at a range of thresholds using the proposed 7-point (H_7), 19-point (H_{19}) and 37-point (H_{37}) Linear-Gaussian hexagonal operators, and for comparison, equivalently sized Shima hexagonal operators ($Shima_7$ and $Shima_{19}$) and near-circular square operators (NC_{3x3}, NC_{5x5}, NC_{7x7},) have been applied to the same set of images. Figure 20 shows an example edge map set (for six different threshold (T)) for the H_7 operator applied to the image shown in Figure 19(e).

26

(a) T=20   (b) T=25   (c) T=30

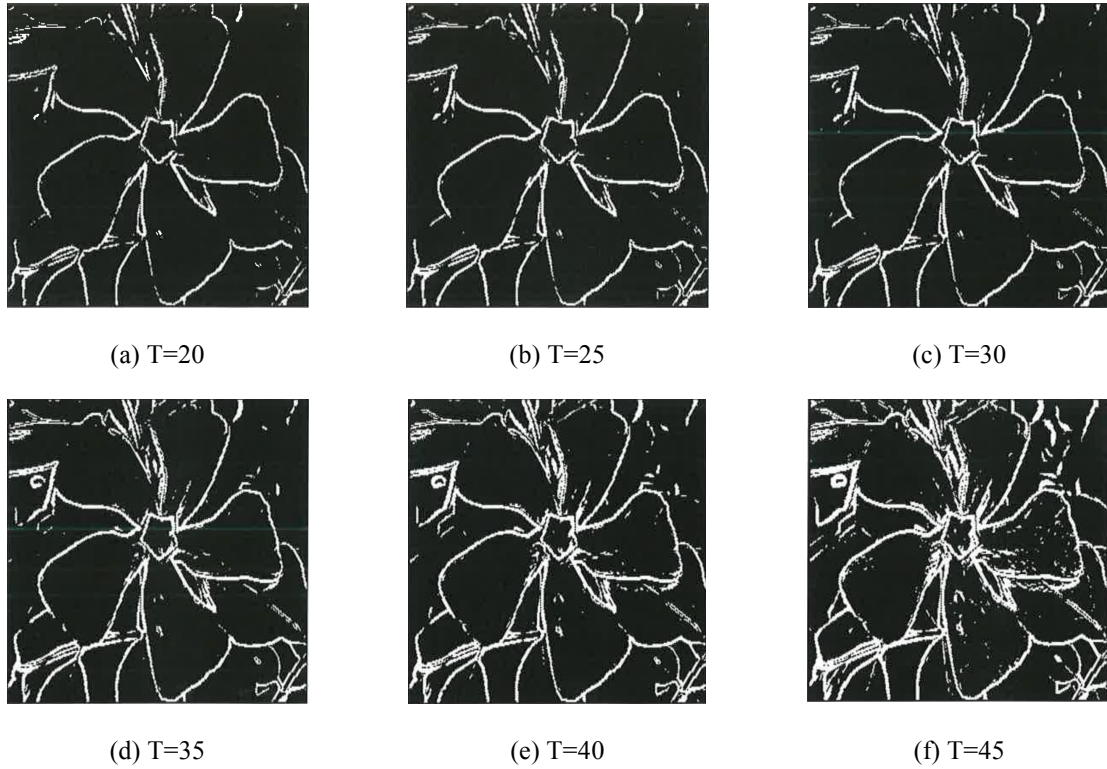(d) T=35   (e) T=40   (f) T=45

Figure 20. An example image set for the H_7 operator at various thresholds values

The information collected from each evaluator was analysed for consistency using an Intraclass Correlation Coefficient. Correlation measures for each operator are presented in Table 4. These results indicate satisfactory consistency between the rankings obtained from the seven human evaluators.

Operator Type	ICC(3,7)
7-point Linear-Gaussian (H_7)	0.7674
7-point Shima (Shima$_7$)	0.8996
3x3 near-circular Square (NC$_{3x3}$)	0.8501
19-point Linear-Gaussian (H_{19})	0.7849
19-point Shima (Shima$_{19}$)	0.8992
5x5 near-circular Square (NC$_{5x5}$)	0.8493
37-point Linear-Gaussian (H_{37})	0.7664
7x7 near-circular Square (NC$_{7x7}$)	0.7612

Table 4: Phase one correlation ratings for each operator

The edge map with the highest mean rating, for each image evaluated by each operator, was selected to be used in phase two of the evaluation. This image set was used to determine which operator performed best overall with respect to detecting edges. Again seven evaluators ranked the image set and consistency was tested using the

Intraclass Correlation Coefficient. The correlation values for phase two are shown in Table 5. Again the values show satisfactory consistency of the data obtained from the evaluators for each operator.

Operator Type	ICC(3,7)
7-point Linear-Gaussian (H_7)	0.6953
7-point Shima ($Shima_7$)	0.8562
3x3 near-circular Square (NC_{3x3})	0.5690
19-point Linear-Gaussian (H_{19})	0.6496
19-point Shima ($Shima_{19}$)	0.8340
5x5 near-circular Square (NC_{5x5})	0.6848
37-point Linear-Gaussian (H_{37})	0.6559
7x7 near-circular Square (NC_{7x7})	0.8565

Table 5: Phase two correlation ratings for each operator

The mean ratings throughout the image set in phase two for each of the evaluated operators are presented in Table 6. These ratings indicate which operator provides the best results when used to detect edges averaged over the set of test images.

Operator Type	Mean Rating
7-point Linear-Gaussian (H_7)	5.500
7-point Shima ($Shima_7$)	4.2857
3x3 near-circular Square (NC_{3x3})	4.7321
19-point Linear-Gaussian (H_{19})	5.4643
19-point Shima ($Shima_{19}$)	4.2143
5x5 near-circular Square (NC_{5x5})	4.6607
37-point Linear-Gaussian (H_{37})	5.2321
7x7 near-circular Square (NC_{7x7})	4.2857

Table 6: Phase two mean rating for each operator

The results show that the proposed 7-point operator has been ranked highest by the evaluators at generating visually pleasing edge maps when compared with an equivalent conventional square operator and the 7-point Shima hexagonal operator. Also the proposed 19-point operator has been ranked highest compared with equivalently sized operators, and the proposed 37-point operator ranked highest when compared with an equivalently sized near-circular operator. These results, combined with the results obtained from the Figure of Merit and Edge Sensitivity Analysis evaluation techniques highlight the improved accuracy obtained when using the proposed hexagonal operator for edge detection.

5. Conclusion

To date, almost all existing hexagonal operators have been developed based on a 7-point neighbourhood, with only the Shima hexagonal operator extending to a larger neighbourhood, i.e. a 19-point neighbourhood (as illustrated in Figure 7). However, as the Shima operator is developed within the frequency domain, it does not readily scale to accommodate larger neighbourhoods in a way that would enable content-adaptive implementation across the image plane. In this paper we have presented a design procedure for hexagonal operators that is easily scalable to any size of neighbourhood, thus enabling content-adaptive implementation. We have illustrated the approach for the case of adaptive first order tri-directional derivative operators with the application of edge extraction and analysis, though other derivative operators, and corresponding applications, may be readily developed within the same framework.

Our comparative evaluation of the proposed Linear-Gaussian hexagonal operators, applied to the tasks of edge extraction and analysis, has embraced a range of techniques, including Figure of Merit, edge sensitivity analysis, and robust visual method. Unlike operators restricted to a single 7-point neighbourhood, the proposed approach is scalable and our results illustrate the relative benefits in terms of improved performance, compared with existing hexagonal operators, when processing images with high levels of noise. To set our hexagonal operator performance into an absolute context, the accuracy of the proposed Linear-Gaussian operators was also compared, at each scale, with finite element based near-circular square operators of equivalent size (operating on a regular rectangular pixel lattice). Results illustrate that, at each scale, the Linear-Gaussian hexagonal operators perform similarly to, and in some cases better than, existing edge detection methods on standard square images. Hence, we conclude that our proposed approach to hexagonal operator design provides acceptable levels of accuracy for hexagonal image processing in absolute terms, whilst readily providing the flexibility to be incorporated into scale-adaptive applications; such flexibility is not easily available through previous hexagonal design techniques.

6. References

[1]   A.P. Paplinski, "Directional Filtering in Edge Detection", IEEE Trans. Image Processing, 7(4) (1998), pp. 611-615.

[2]   B.W. Scotney, S.A. Coleman, "Improving Angular Error via Systematically Designed Near-circular Gaussian-based Feature Extraction Operators", Pattern Recognition 40(5) (2007), pp.1451-1465.

[3] Balakrishnan, M., Pearlman, W., "Hexagonal Sub-band Image Coding with Perceptual Weighting", Optical Engineering , Vol. 32 (1993), pp. 1430-1437.

[4] C.A. Wüthrich, P. Stucki, "An algorithmic comparison between square- and hexagonal-based grids", CVGIP: Graphical Model and Image Processing, 53(4) (1991), pp. 324-339.

[5] Curcio, C., Sloan, K., Kalina, R., & Hendrickson, A, "Human Photoreceptor Topography", The Journal of comparative neurology , Vol. 292 (4) (2004), pp. 497-523.

[6] E.R. Davies, "Circularity – A New Design Principle Underlying the Design of Accurate Edge Orientation Filters", Image and Vision Computing 5 (1984), pp. 134-142.

[7] Gardiner, B., Coleman, S.A. and Scotney, B.W., "Comparing Hexagonal Image Resampling Techniques with Respect to Feature Extraction", In: 14th International Machine Vision and Image Processing Conference, University of Limerick. Cambridge Scholars, (2011), pp. 102-115.

[8] He, X., & Jia, W., "Hexagonal Structure for Intelligent Vision. Information and Communication Technologies", First International Conference, (2005), pp. 52-64.

[9] Huang, C., & Lin, C., "Bio-inspired Computer Fovea Model based on Hexagonal-type Cellular Neural Network", IEEE Transactions on Circuits and Systems I: Regular Papers , Vol. 54 (1) (2007), pp. 35-47.

[10] J.D. Allen, "Filter Banks for Images on Hexagonal Grid", Signal Solutions, (2003).

[11] Jiang, Q., "Orthogonal and Biorthogonal FIR Hexagonal Filter Banks with Sixfold Symmetry", IEEE Transactions on Signal Processing , Vol. 56 (2008), pp. 5861-5873.

[12] Kitchen, L., Malin, J., "The Effect of Spatial Discretization on the Magnitude and Direction Response of Simple Differential Edge Operators on a Step Edge", Computer vision, graphics, and image processing, Vol. 47 (2) (1989), pp. 243-258.

[13] Knaup, M., Steckmann, S., Bockenbach, O., & Kachelries, M., "CT Image Reconstruction using Hexagonal Grids", IEEE Medical Imaging Conference Rec , Vol. 13 (2007), pp. 2074-3076.

[14] L. Kitchen, J. Malin, "The Effect of Spatial Discretization on the Magnitude and Direction Response of Simple Differential Edge Operators on a Step Edge", Computer Vision, Graphics, and Image Processing, Vol. 47 (1989), pp. 243-258.

[15] L. Middleton, J. Sivaswamy, "Edge Detection in a Hexagonal-Image Processing Framework, Image and Vision Computing" 19 (2001), pp. 1071-1081.

[16] L. Middleton, J. Sivaswamy, "Hexagonal Image Processing; A Practical Approach", Springer, (2005).

[17] Lau, D., & Ulichney, R., "Blue-noise Halftoning for Hexagonal Grids" IEEE Transactions on Image Processing, Vol. 15 (2006), pp. 1270-1284.

[18] M. Heath, S. Sarkar, T. Sanocki, K. Bowyer, "A Robust Visual Method for Assessing the Relative Performance of Edge-detection Algorithms", IEEE Transactions on Pattern Analysis and Machine Intelligence, Vol. 19 (1997), pp. 1338-1359.

[19] M.A. Ruzon, C. Tomasi, "Colour Edge Detection with the Compass Operator, Computer Vision and Pattern Recognition", Vol. 2 (1999), pp. 166-169.

[20] Q. Wu, X. He, T. Hintz, "Bi-lateral filtering based edge detection on hexagonal architecture", Proc. IEEE Int. Conference Acoustics, Speech, and Signal Processing, (2005), pp. 713- 716.

[21] Q. Wu, X. He, T. Hintz, "Virtual Spiral Architecture", International Conference on Parallel and Distributed Processing Techniques and Applications, (2004), pp. 339-405.

[22] Qiang, W. J., "Uniform Image Partioning for Fractial Compression on Virtual Hexagonal Structure", International Journal of Information and Systems Sciences , Vol. 3 (2007), pp. 492-509.

[23] R. Vitulli, "Aliasing Effects Mitigation by Optimized Sampling Grids and Impact on Image Acquisition Chains", Geoscience and Remote Sensing Symposium, (2002), pp. 979-981.

[24] R.C. Staunton, "The design of hexagonal sampling structures for image digitisation and their use with local operators", Image Vision Computing, Vol. 7(3) (1989), pp. 162-166.

[25] S. Ando, "Consistent Gradient Operators", IEEE Trans. Pattern Analysis and Machine Intelligence, Vol. 22(3) (2000), pp. 252-265.

[26] S. Ghiasi, R. Safabakhsh, "Omnidirectional Edge Detection", Computer Vision and Image Understanding, Vol. 113 (2009), pp. 556-564.

[27] S.A. Coleman, B.W. Scotney, M.G. Herron, "A Systematic Design Procedure for Scalable Near-Circular Laplacian of Gaussian Operators", Proc. of Int. Conference on Pattern Recognition, Cambridge, (2004), pp. 700-703.

[28] Shimonomura, K., Kushima, T., & Yagi, T., "Neuromorphic Binocular Vision System for Real-time Disparity Estimation", IEEE International Conference on Robotics and Automation, (2007), pp. 4867-4872.

[29] Staunton, R.C., "The Design of Hexagonal Sampling Structures for Image Digitisation and Their Use with Local Operators", Image and Vision Computing, pp. 162-166.

[30] T. Shima, S. Saito, M. Nakajima, "Design and Evaluation of More Accurate Gradient Operators on Hexagonal Lattices", IEEE Trans. Pattern Analysis and Machine Intelligence, Vol. 32(6) (2010), pp. 961-973.

[31] Thiem, J., & Hartmann, G., "Biology-inspired Design of Digital Gabor filters upon a Hexagonal Sampling Scheme", ICPR, (2000) pp. 3449-3554.

[32] W.K. Pratt, "Digital Image Processing", John Wiley & Sons Inc., Second Edition, (1991).

[33] Wu, Q., He, X., & Hintz, T., "Virtual Spiral Architecture", International Conference on Parallel and Distributed Processing Techniques and Applications , Vol. 1 (2004), pp. 399-405.

[34] X. He, W. Jia, "Hexagonal Structure for Intelligent Vision", Information and Communication Technologies (2005), pp. 52-64.